

An Improved Method for Reconstructing the Digital Core Model of Heterogeneous Porous Media

Lili Ji¹ · Mian Lin^{1,2} · Wenbin Jiang¹ · Chenjie Wu¹

Received: 2 January 2017 / Accepted: 13 November 2017 / Published online: 22 November 2017
© Springer Science+Business Media B.V., part of Springer Nature 2017

Abstract The heterogeneous pore space of porous media strongly affects the storage and migration of oil and gas in the reservoir. In this paper, the cross-correlation-based simulation (CCSIM) is combined with the three-step sample method to reconstruct stochastically 3D models of the heterogeneous porous media. Moreover, the two-point and multiple-point connectivity probability functions are used as vertical constraint conditions to select the boundary points of pore and matrix, respectively. The heterogeneities of pore spaces of four rock samples are investigated, and then our methods are tested on the four samples. Quantitative comparison is made by computing various statistical and petrophysical properties for the original samples, as well as the reconstructed model. It was found that the results from CCSIM-TSS are obviously better than that from CCSIM. Finally, the analysis of the distance (ANODI) was used to measure of the variability between the realizations of the four rock samples. The results demonstrated that the results from CCSIM-TSSmp are better than that from CCSIM-TSSsp as the complexity of connectivity and heterogeneities of pore spaces increase.

Keywords Reconstruction · CCSIM-TSS · Multiple connectivity · Heterogeneous porous media

1 Introduction

Pore space is the petroleum migration pathways and reservoir space, and its morphology (the geometry and the connectivity) can strongly affect the storage and migration of oil and gas in the reservoir (Weger et al. 2009; Payne et al. 2010). On the other hand, as microscopic

✉ Mian Lin
linmian@imech.ac.cn

¹ Key Laboratory for Mechanics in Fluid Solid Coupling Systems, Institute of Mechanics, Chinese Academy of Sciences, Beijing 100190, China

² University of Chinese Academy of Sciences, Beijing 100190, China

structure is gradually becoming the center of interest in recent years, the heterogeneity of the porous media stands out. Hence, it is of great significance to accurately describe the pore structure of heterogeneous porous media.

Methods based on stochastic or geostatistical simulation have been developed to reconstruct digital cores, which can describe the pore structure. In general, reconstruction methods that are commonly used at present are process-based methods, simulated annealing method, Gaussian random fields, single normal equation simulation method (SNESIM), etc. Process-based methods (Bryant and Blunt 1992; Biswal et al. 1999, 2007; Coelho et al. 1997; Øren and Bakke 2002, 2003) try to develop 3D models by mimicking the physical processes that form the porous medium. Though realistic, such methods are, however, computationally expensive and require considerable calibrations. Moreover, they are not general enough, because each of them is developed for a specific type of rock, as each type is the outcome of some specific physical processes. Simulated annealing method uses statistical information drawn from the porosity and the two-point autocorrelation function of 2D images to regenerate 3D images (Hazlett 1997). However, this method fails to reproduce the long-range connectivity of the pore space, especially for low porosity materials and particulate media with special shapes, because only the low-order information is used (Mo et al. 2016). The method based on a truncated Gaussian random field is often used with the geometrical properties of the original pore space to reconstruct 3D images (Quiblier 1984; Ioannidis et al. 1999; Thovert et al. 2001; Thovert and Adler 2011). These geometrical properties include porosity, two-point correlation function, local porosity distribution, local percolation probability, etc. Like simulated annealing method, this method is also difficult to reproduce the long-range connectivity of the pore space. The single normal equation simulation (SNESIM) proposed by Strebelle (2002) and Strebelle and Cavelius (2014) uses a search tree structure, an efficient method of accessing high-dimensional data that can overcome the problems associated with the original MPS method. The method is computationally demanding and unable to control the continuity and variability among adjacent layers (Hajizadeh et al. 2011; Hajizadeh and Farhadpour 2012). Recently, based on SNESIM, Gao et al. (2015) proposed a three-step sampling algorithm in which the edge area is extracted based on a two-point correlation function during reconstructing each layer of the 3D models. This method can preserve the long-range (global) connectivity of the pore space in the vertical direction (perpendicular to the layers reconstructed or the direction in which the layers are stacked). Although the previously described methodologies are available for homogeneous porous media (such as sandstones), none of them is capable of reconstructing accurately heterogeneous and anisotropic porous media (such as carbonate rock and shales).

In recent years, several methods have been developed to reconstruct heterogeneous porous media. Yao et al. (2013) used simulated annealing method and Markov Chain Monte Carlo method to reconstruct the macropore digital rock and micropore digital rock, respectively, and then the two types of digital cores are superposed together according to a superposition algorithm. Recently, the cross-correlation-based simulation (CCSIM) method, proposed by Tahmasebi et al. (2012, 2015, 2016), was used to reconstruct stochastically equiprobable 3D models of shale rocks. This method produces an ensemble of 3D realizations that provide acceptable approximation of the same properties in the 2D image(s). However, the reconstructed vertical morphological features are unsatisfactory (Gao et al. 2015; Tahmasebi and Sahimi 2016), and also the method is unable to reproduce accurately the experimental data for the permeability and electrical conductivity. Thus, in this paper, to reproduce accurately the strong heterogeneity of the pore space of porous media, we combine the cross-correlation-based simulation (CCSIM) with the three-step sampling algorithm to improve the accuracy of the CCSIM algorithm. The improved methodology in this paper is named as CCSIM-TSS.

The rest of this paper is organized as follows. In the next section, the improved methodology (CCSIM-TSS) is described in detail. In the CCSIM-TSS algorithm, the two-point and multiple-point connectivity probability functions are used as constraint conditions to select the boundary points during reconstructing each layer, respectively. To make a distinction, the former is indicated by CCSIM-TSS_{tp}, and the later by CCSIM-TSS_{mp}. Then, the accuracy of the new algorithms is tested using several heterogeneous rock samples. Finally, the paper concludes with a summary and discussion of the results

2 Methodology

2.1 Heterogeneous Rock Samples

2.1.1 The Heterogeneous Porous Media Usually have a Wide Size Range of Pores and Complex Connectivity

In order to investigate the reconstruction of heterogeneous porous media, we select four typical rock samples (C1, C2, C3, and C4) for reconstruction. C1, C2 and C3 are carbonate rocks, and C4 is sandstone. The petrophysical properties of the four samples are listed in Table 1. It is necessary to point out that the permeabilities in Table 1 are absolute permeabilities (k_x , k_y and k_z) computed by LBM (Lattice Boltzmann Method). In the following, we will investigate the connectivity and the structures of the pore spaces of the four samples.

At first the Micro-CT image, the relation between the sample size and porosity, the multiple-point and two-point connectivity probability functions of the four rock samples are shown in Fig. 1. As Fig. 1 indicates, the porosity of each rock sample exhibits strong fluctuations when the sample size is very small, reaching a plateau when the sample size is bigger than 100 pixels. Thus, it can be obtained that the sizes of the four rock samples (C1, C2, C3 and C4) in our paper are sufficient to contain a representative elementary volume (REV). Furthermore, the multiple-point connectivity probability functions of different sample sizes for each rock sample are normalized and plotted together. It can be found that as the sample size increases, the corresponding multiple-point connectivity probability function is gradually close together. In particular, when the sample sizes for each rock sample are bigger than 100 pixels, the multiple-point connectivity probability functions have a tiny discrepancy with each other. We can obtain that the connectivity of the rock sample reach a plateau when the sample size are sufficient to contain a REV.

Table 1 The petrophysical properties of the four rock samples

	C1	C2	C3	C4
Size	200 × 200 × 200	200 × 200 × 200	200 × 200 × 200	300 × 300 × 300
Resolution (μm)	10.69	5.7	1.016	9.1
Porosity (%)	16.8	23.3	12.8	16.9
k_x (mD)	160	785	48	815
k_y (mD)	380	1469	20	1363
k_z (mD)	205	1053	7	875

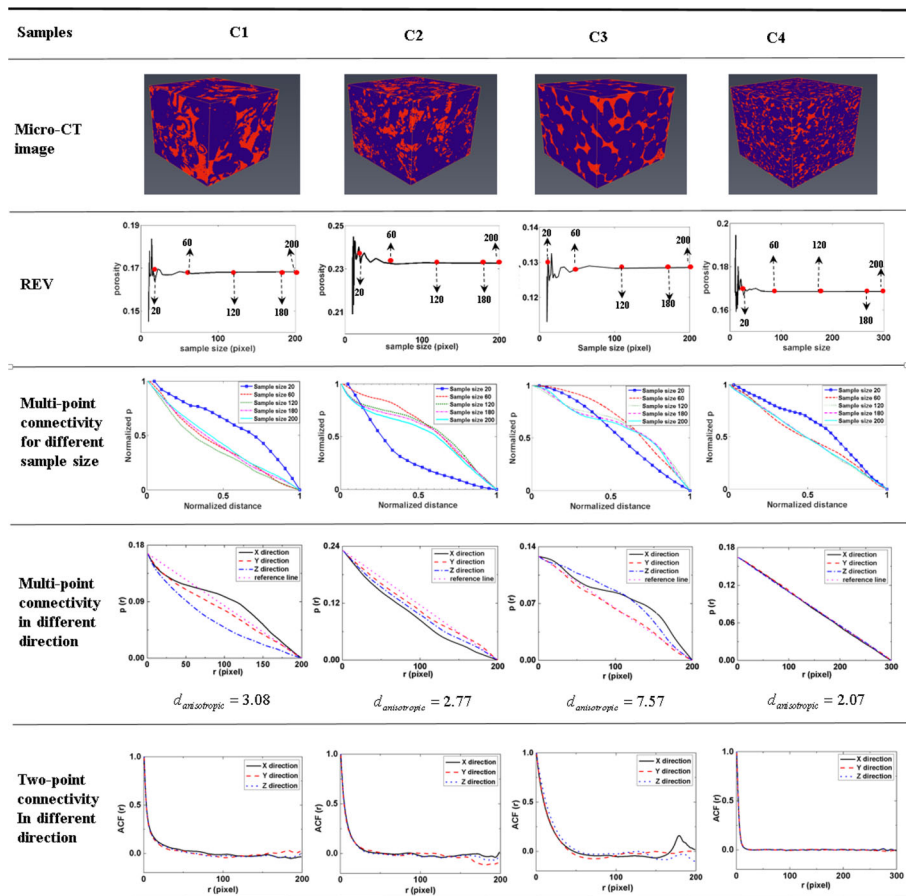


Fig. 1 The Micro-CT image, the multiple-point connectivity probability and the two-point connectivity probability of the four samples

Now we discuss the connectivity of the pore spaces of the four rock samples based on the multiple-point and two-point connectivity probability function (see “Appendix”). To compare the connectivity in different directions, Fig. 1 shows the two-point and multiple-point connectivity probability functions ($ACF(r)$ and $P(r)$) of the samples in three directions. It can be seen from Fig. 1 that the multiple-point connectivity probability functions of C1, C2 and C3 in different directions have a significant difference. It indicates that the first three samples are typically anisotropic, while the last one is isotropic. To compare the anisotropy of the four rock samples quantitatively, the reference line, defined as the straight line between the beginning and the end point of the multiple-point connectivity probability curve, is introduced. The difference between the multiple-point connectivity probability curve in each direction and the reference line of the rock sample are computed, and denoted as dx , dy and dz . $d_{\text{anisotropic}}$ is the ratio of the max and min of dx , dy and dz , and as $d_{\text{anisotropic}}$ increases, the anisotropy of the rock sample become stronger. $d_{\text{anisotropic}}$ of the four rock samples are listed in Fig. 1, and it can be deduced that the sample C3 has the strongest anisotropy, followed by C1 and C2. Then, we investigate the two-point connectivity probability functions of the four rock samples. Figure 1 demonstrates that there is only a small difference in the two-point

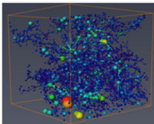
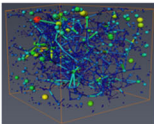
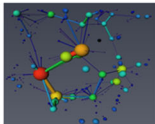
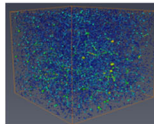
Samples	C1	C2	C3	C4	
Pore Network					
Pore size	σ	9.44E-06	7.43E-06	1.30E-06	8.03E-06
	E	2.15E-05	1.34E-05	1.38E-06	2.17E-05
	$V(\frac{\sigma}{E})$	4.38E-01	5.54E-01	9.42E-01	3.70E-01
Pore-throat Ratio	R_{pt}	2.48E-03	9.12E-03	6.27E-02	4.71E-04

Fig. 2 The pore network of the four samples, the mean (E), variance (σ) and the ration between variance and mean (V) of the pore-size distribution, the percentage of high pore-throat ratio (> 10)

connectivity probability functions of different directions for the four samples. Thus, we can conclude that the multiple-point connectivity probability function can characterize the spatial continuity of the structure of heterogeneous porous media more accurately than the two-point connectivity probability function. This is because that the two-point connectivity probability function does not take into account the curvilinearity of the structures (Krishnan and Journel 2003). Considering that the heterogeneous porous media usually have complex connectivity, we introduce the multiple-point connectivity probability function as the constraint condition in the CCSIM-TSS algorithm.

Then, the structures of the pore spaces of four rock samples are examined. The pore network of the four samples are extracted by a newly developed pore network extraction algorithm, the AB (axis & ball) algorithm (Yi et al. 2017), as shown in Fig. 2. Then, the pore-size distribution of the samples are calculated to investigate the heterogeneity of pore spaces of the four rock samples quantitatively. Figure 2 compares the mean (signed by E), variance (signed by σ) and the ration between variance and mean (signed by V) of the pore-size distribution of the four rock samples. A striking feature of Fig. 2 is that the sample C3 has the biggest value of V , indicating that C3 has the widest size range of pores and its pore space is the most heterogeneous one in the four samples. We can also deduce that the pore space of C4 is the most homogeneous one and the pore space of C1 is more homogeneous than C2. Furthermore, the pore-throat ratio, the ratio of pore radius to the linked throat radius, is also calculated to investigate the heterogeneity of pore space. The percentage of high pore-throat ratio which is bigger than 10, signed by R_{pt} , are shown in Fig. 2. It can be found that R_{pt} of C4 is smaller than the other three samples, indicating that the difference between pore sizes and throat sizes of C4 is smaller than the other three samples and C4 is more homogeneous. In summary we can conclude that the pore space of C3 is the most heterogeneous one, followed by C2, C1 and C4.

From the above discussion, we can see that the pore spaces of the four rock samples are typically inhomogeneous. Thus, we will use the four samples for reconstruction in the following section.

2.2 CCSIM-TSS Method

The improved method, CCSIM-TSS, combines the cross-correlation-based simulation (CCSIM) with the three-step sampling method together to reconstruct stochastically 3D

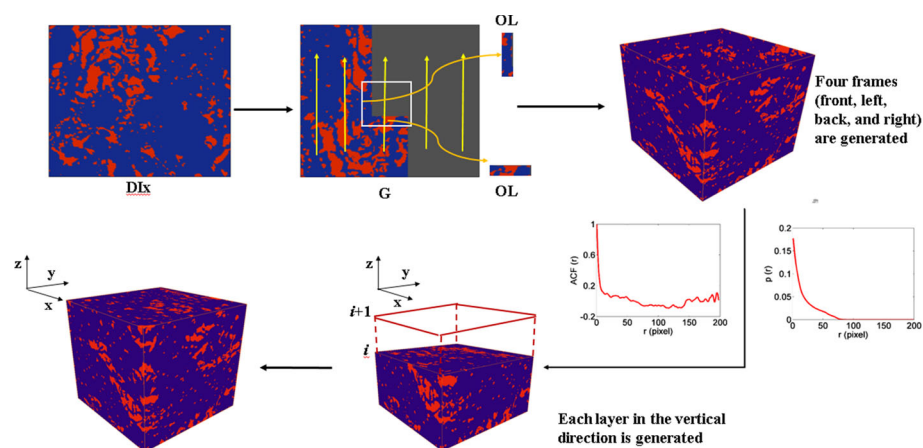


Fig. 3 The description of the CCDIM-TSS algorithm

models of the heterogeneous porous media. The specific steps of CCSIM-TSS are arranged as follows (as show in Fig. 3).

1. At first, typical digital images (DIs) in three directions (DI_{xy} , DI_{yz} and DI_{xz}), which include most of the expected variations and heterogeneity of a porous medium, are selected.
2. Let G represent the simulation grid that is used to reconstruct a model. Then, G is partitioned into small blocks or templates T , while the data event at position $u(x, y)$ in T —the data that are sampled and inserted in T —is denoted by $DT(u)$. The data inserted in a template may change during the reconstruction, until the realization is completely developed. As described, the conceptual information is presented as a DI. Figure 3 shows an example of a DI. The simulation starts from a corner of the grid G and proceeds along a 1D raster path as shown by the yellow arrows in Fig. 3. At each step, to preserve the continuity between the patterns, an overlap region OL, populated with information from the DI, is extracted from G , and its similarity with the DI is evaluated by calculating the CCF (Tahmasebi et al. 2012, 2015, 2016):

$$C(i, j; x, y) = \sum_{x=0}^{l_x-1} \sum_{y=0}^{l_y-1} DI(x+i, y+j) DT(x, y) \quad (1)$$

where $0 \leq i < L_x + l_x - 1$ and $0 \leq j < L_y + l_y - 1$. $DI(x, y)$ represents the location at point (x, y) of DI of size $L_x \times L_y$, with $x \in \{0, \dots, L_x - 1\}$ and $y \in \{0, \dots, L_y - 1\}$. The OL region of size $l_x \times l_y$ and data event DT is used to match the pattern in the DI . Finally, one of the acceptable candidate patterns is selected and inserted in the current DT in G . The acceptance criterion is based the CCF and a threshold defined for it that the CCF must exceed.

The original DI_{xy} is set as the first layer at the bottom of 3D model Then, the other four frames (i.e., front, left, back, and right) are generated using the method described above, as shown in Fig. 3. Next we start to reconstruct each layer in the vertical direction (z direction).

3. During generating each layer in the vertical direction, we use the three-step sampling method to extract the conditional data. Firstly, the two-point connectivity probability

Table 2 The edge sampling procedure based on the two- and multiple-point connectivity probability function

1. Calculate the number of pores (N_p) that should be selected from the boundary points of pore and the matrix and isolated points 2. Obtain the array of the boundary points of pore and the matrix and isolated points $e(x,y)$ from the reconstructed part	
3. For $r=L_i$; $r \geq 1$; $r = r - 1$ 4. Calculate the two-point connectivity probability function (ACFrec(r)) of the reconstructed part $c(x,y,z)$ ($0 \leq x < W$, $0 \leq y < H$, $0 \leq z < L_i$) 5. For $(x_0, y_0) \in e(x,y)$ 6. If ACFrec(r) > ACF(r); $c(x_0, y_0, z-r) = \text{pore}$; $e(x_0, y_0) = \text{pore}$ 7. Delete (x_0, y_0) 8. ++count 9. Elseif ACFrec(r) < ACF(r); $c(x_0, y_0, z-r) = \text{grain}$; $e(x_0, y_0) = \text{grain}$ 10. Delete (x_0, y_0) 11. ++count 12. If the number of pores in $e(x,y)$ -count < N_p 13. Break; 14. End 3;	3. For $(x_0, y_0) \in e(x,y)$ 4. Calculate the multiple-point connectivity probability function in XZ and YZ Plane passing through the point (x_0, y_0) of the reconstructed part $c(x,y,z)$ ($0 \leq x < W$, $0 \leq y < H$, $0 \leq z < L_i$), signed by $Px(r)$ and $Py(r)$ 5. For $r=L_i$; $r \geq 1$; $r = r - 1$ 6. If $Px(r) > P(r)$; $Py(r) > P(r)$; $e(x_0, y_0) = \text{pore}$ 7. Delete (x_0, y_0) 8. ++count 9. Elseif $Px(r) < P(r)$; $Py(r) < P(r)$; $e(x_0, y_0) = \text{grain}$ 10. Delete (x_0, y_0) 11. ++count 12. If the number of pores in $e(x,y)$ -count < N_p 13. Break; 14. End 3;
15. Count the number of pores in $e(x,y)$, and signed by s , 16. If $s > N_p$ 17. Select sampling point N_p from s randomly 18. Else 19. Set the pore phase points in $e(x,y)$ as sampling points, then select $N_p - s$ pore phase sampling points from the deleted points randomly 20. Select sampling points with grain phase as the steps 1–19	

function (ACF(r)) and the multiple-point connectivity probability function ($P(r)$) are calculated based on the typical digital images (DIs), as shown in Fig. 3. Let $i + 1$ be the number of layers to be reconstructed currently. Now we select the hard data based on the three-step sampling method. In the first step, the i th layer is scanned using a 5×5 sampling template; the central node of the template, which is entirely pore (grain), is marked as a sampling point, the number of sampling points is recorded, and this sampled area is labeled. Then, the remaining portion of the image is scanned using a 3×3 sampling template, and the process stated before is performed again. In the second step, the unavailable sampling area is labeled, and the number of pixels is recorded. In the third step, the edge area is marked. The sampling points in the edge area are selected according to the algorithm described in Table 2. It should be noted that the edge sampling method based on the two-point connectivity probability function is different from that based on the multiple-point connectivity probability function. In the former method, the ACF of the 3D reconstructed part is calculated and then is compared with the ACF of DIs to sample the edge points. However, in the later method, the multiple-point connectivity probability functions of the XZ plane and YZ plane passing through the edge point, denoted by $Px(r)$ and $Py(r)$, are calculated, respectively, and then are compared with the $P(r)$ of DIs to determine whether the edge point is selected. Finally, all of the selected sampling points are shown in Fig. 4c, where the edge points are sampled based on the multiple-point connectivity probability function.

The procedure continues until all the (2D) layers have been reconstructed. Eventually, all the generated layers are stacked together to create the reconstructed 3D model.

- Finally, we use an iterative scheme to increase the similarity between the existing features in the reconstructed 3D model and the DIs. For each voxel in the reconstructed model, three different patterns (qx , qy , qz) in three orthogonal planes passing through the voxel are selected. The CCF between the patterns and the corresponding entire 2D DIs image are computed, and thus the closest patterns (p_x , p_y , p_z) corresponding to (qx , qy , qz) are selected, as shown in Fig. 5. Then, each selected pattern p_x , p_y , and p_z is inserted into

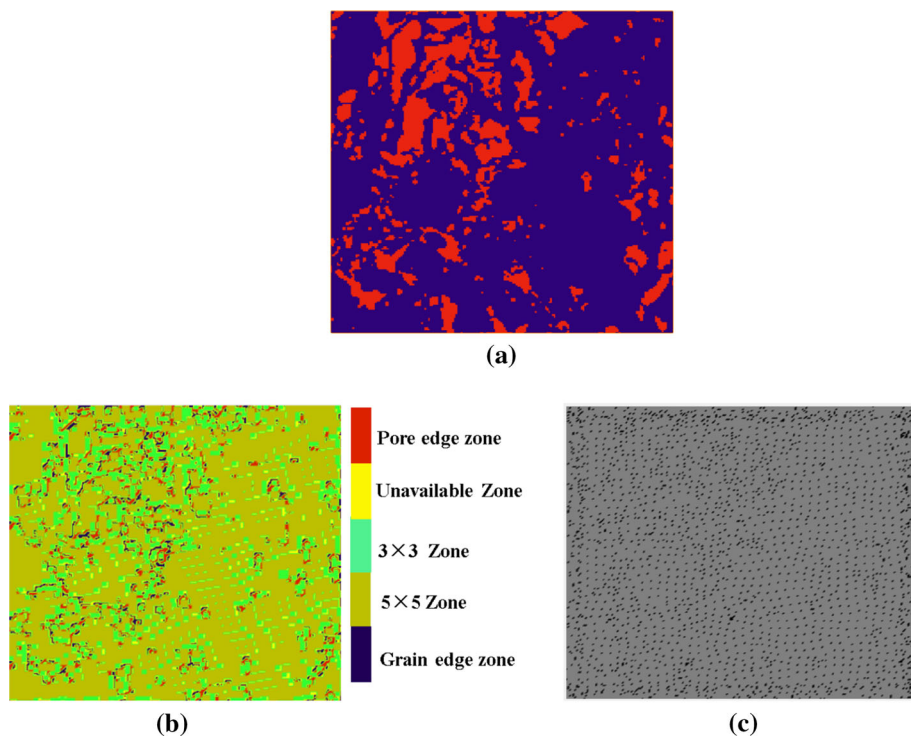


Fig. 4 The i th imaging (a); the procedure of three-step sampling (b); the final selected sampling points (c)

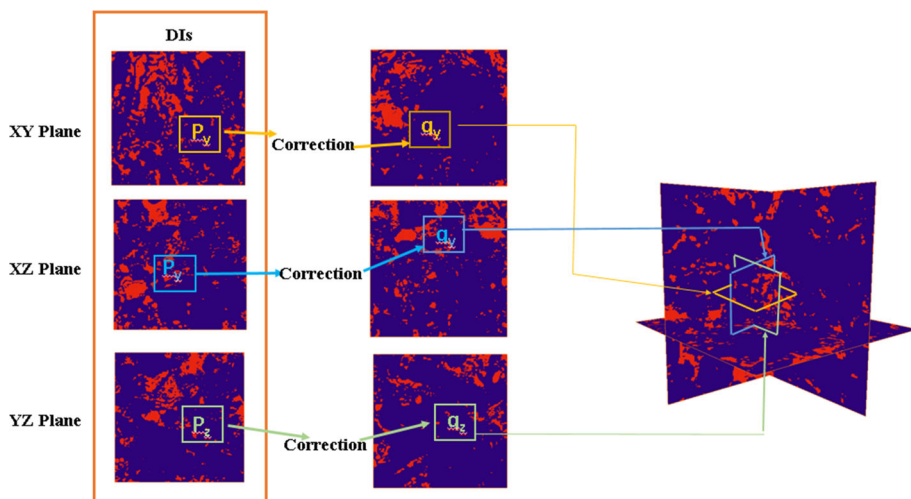


Fig. 5 Iterative 3D modeling: extraction of three data events in output 3D model (q_x, q_y, q_z), with the best three candidates (p_x, p_y, p_z) being found in the DIs

the 3D model, the histogram of the 3D model is constructed. Then, the Jensen–Shannon distance $d_{JS}(p, q)$ between the resulting histograms of the three patterns (p_i) within the reconstructed 3D model with the DIs is calculated, as shown in Eq. 2. The one that has

the minimum $d_{JS}(p, q)$ is selected as the final value of the voxel in the 3D model. The above steps are repeated until all of the voxels in the 3D mode are visited.

$$d_{JS}(p, q) = \frac{1}{2} \sum_i p_i \log \left(\frac{p_i}{q_i} \right) + \frac{1}{2} \sum_i q_i \log \left(\frac{q_i}{p_i} \right) \quad (2)$$

For the sake of discussion, the algorithm that uses two-point connectivity probability functions as constraint conditions is named as CCSIM-TSStp, while the algorithm that uses multiple-point connectivity probability functions as constraint conditions is named as CCSIM-TSSmp.

3 Results and Discussion

In this section, we use the improved method (CCSIM-TSS) to reconstruct the four typical heterogeneous porous media in the above section.

3.1 Verification

The first sample, referred to as C1, is selected for reconstruction. In this first numerical experiment, we focus our attention on comparing the CCSIM-TSS algorithm with the algorithm CCSIM. The 2D images of C1 used as DIs are shown in Fig. 6. Because of the heterogeneity of the sample C1, patterns in each direction are different. Also, based on the three DIs, the two-point connectivity probability function ($ACF(r)$) and the multiple-point connectivity probability function ($P(r)$) are extracted, as shown in Fig. 7. And they will be used as vertical constraint conditions in CCSIM-TSStp and CCSIM-TSSmp, respectively.

The realizations generated by CCSIM, CCSIM-TSStp and CCSIM-TSSmp are shown in Fig. 8. As they manifest, the reconstructed results have reproduced the structure and connectivity of the original sample. At the visual level, the three methods are capable of preserving the connectivity of the sample in the direction of stacking the 2D images that it reconstructs, as well as the variability in the spatial distribution of the pores.

To further examine the three algorithms, we generate 30 realizations using each algorithm and then use the MDS-ANODI (the multidimensional-scale and the analysis of the distance) to analyze the results (Tan et al. 2014). The Jensen–Shannon divergence is used to calculate the distances m_{ij} between each pair of realizations and the distances between realizations and the Micro-CT image. Thus, a 91×91 distance matrix (M) can be constructed, and

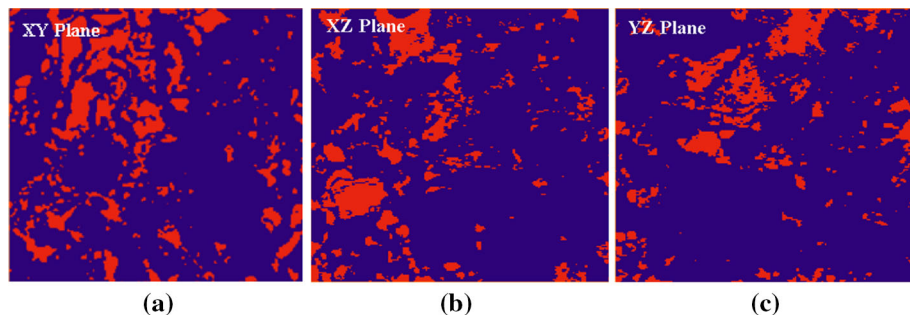


Fig. 6 The extracted 2D representative DIs in the x , y and z directions

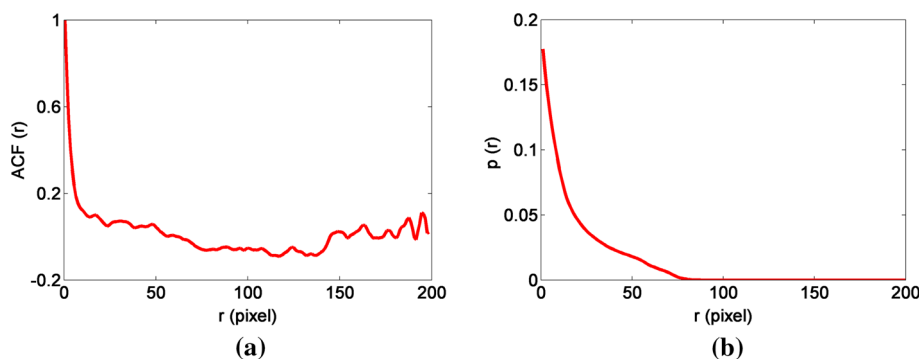


Fig. 7 The two-point connectivity probability function (a) and the multiple-point connectivity probability function (b)

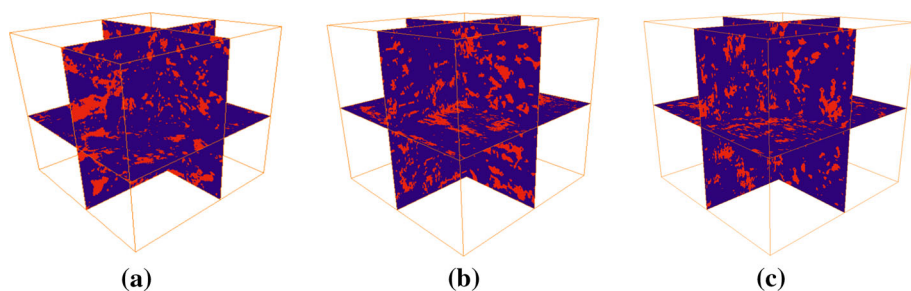


Fig. 8 Three reconstructed models by CCSIM (a), CCSIM-TSStp (b) and CCSIM-TSSmp (c)

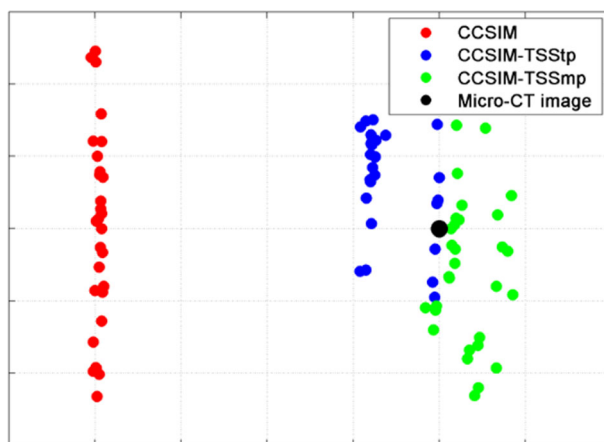
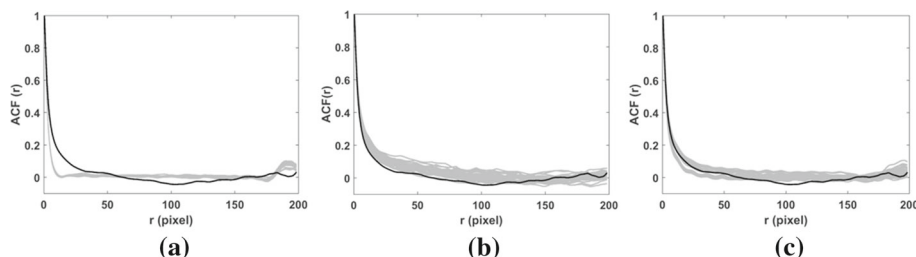


Fig. 9 The MDS-ANODI plot illustrating the spatial variability. Realizations (shown here by green for the CCSIM-TSSmp and by blue for the CCSIM-TSStp) with better pattern reproduction are distributed around the Micro-CT image (the black dot)

then, it is visualized using the MDS (Multidimensional scaling), as shown in Fig. 9. MDS relies on eigenvalue decomposition; the x -axis in Fig. 9 refers to the largest eigenvalue of the distance matrix (M), the y -axis to the second largest eigenvalue. The units on these axes

Table 3 The ANODI scores for the variability of within and between realizations and total ratio for the newly proposed CCSIM-TSStp, CCSIM-TSSmp and CCSIM

Space of uncertainty (between)	CCSIM-TSSmp:CCSIM-TSStp:CCSIM	1:0.7606:0.9348
Pattern reproduction (within)	CCSIM-TSSmp:CCSIM-TSStp:CCSIM	1:0.8175:1.3025
Ratio (between/within)	CCSIM-TSSmp:CCSIM-TSStp:CCSIM	1:0.9305:0.7177

**Fig. 10** Comparison of the two-point connectivity probability for the CT image (black) and reconstructed models (gray). **a** CCSIM; **b** CCSIM-TSStp; **c** CCSIM-TSSmp

are not important; what matters are relative distances between these points (Tan et al. 2014). The better pattern reproduction of the CCSIM-TSS (CCSIM-TSStp and CCSIM-TSSmp) algorithm is well illustrated in this plot, as most of the green and blue dots, corresponding to the CCSIM-TSS realizations, are distributed closer to the Micro-CT image (black dot). To further quantify the accuracy of the CCSIM-TSS method, the results of the ANODI analysis (the analysis of the distance) are summarized in Table 3, where space of uncertainty (between-realization variability) refers to the result for the distances between the realizations, whereas pattern reproduction (within-realization variability) represents the result for the distances between the realizations and the Micro-CT image. Tan has pointed out that the best algorithm should minimize the within-realization variability and at the same time maximize the variability between the produced realizations. As a result, the best algorithm is expected to have the largest ratio (between/within) (Tan et al. 2014). The ratio of space of uncertainty and pattern reproduction is denoted as γ . Thus, Table 3 demonstrates that the uncertainty space of the CCSIM-TSS generated realizations is shrunk trivially, whereas the pattern reproduction is improved tremendously. Furthermore, $\gamma_{\text{CCSIM-TSSmp}}:\gamma_{\text{CCSIM-TSStp}}:\gamma_{\text{CCSIM}}$ is 1:0.9305:0.7177 meaning that the CCSIM-TSS algorithm performs better than CCSIM.

Next we compare the connectivity of the micro-CT image of C1 and the reconstructed results from the CCSIM-TSS (CCSIM-TSStp and CCSIM-TSSmp) and CCSIM algorithm. The two-point connectivity probability function are computed. The comparisons for the micro-CT medium of C1 and reconstructed results are presented in Fig. 10. It is clear that the two-point connectivity probability function of the reconstructed results from the CCSIM-TSS algorithm match the actual data better than that from the CCSIM algorithm.

Now consider the pore-size distribution of the reconstructed results. Figure 11 displays the pore-size distributions of the realizations generated by the three algorithms and the micro-CT image of C1. It is also clear that there is a very good agreement between the realizations generated by CCSIM-TSS algorithm and the micro-CT image. The CCSIM-TSS algorithm can reproduce the pore-size distributions better than the CCSIM algorithm, while CCSIM-TSSmp has a slightly better results than CCSIM-TSStp.

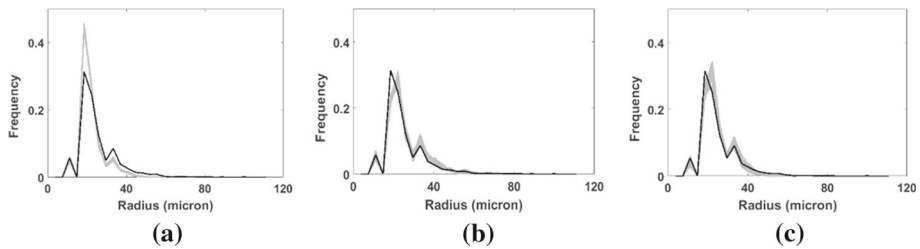


Fig. 11 The pore-size distribution of the reconstructed results (gray) and the Micro-CT image (black). **a** CCSIM; **b** CCSIM-TSSp; **c** CCSIM-TSSmp

Table 4 Comparison of the absolute permeabilities for the reconstructed results generated by the CCSIM, CCSIM-TSSp and CCSIM-TSSmp method

	CCSIM			CCSIM-TSSp			CCSIM-TSSmp		
	k_x (mD)	k_y (mD)	k_z (mD)	k_x (mD)	k_y (mD)	k_z (mD)	k_x (mD)	k_y (mD)	k_z (mD)
Max	1451	1566	832	168	1202	482	605	2100	461
Upper quartile	1176	1487	686	97	783	295	493	1446	255
Lower quartile	977	1378	583	48	295	147	137	344	130
Min	856	1275	515	0	63	46	87	183	41
Median	1089	1440	651	64	475	211	253	456	204

Finally, the absolute permeabilities of the realizations in three directions from the CCSIM-TSS (CCSIM-TSSp and CCSIM-TSSmp) and CCSIM algorithm are computed (Table 4). The absolute permeabilities of the Micro-CT image of C1 are $k_x = 160$ mD, $k_y = 380$ mD and $k_z = 205$ mD, which are listed in Table 1. Comparing the median permeabilities in Table 4 with the results of the Micro-CT image, we find that the realizations generated by CCSIM-TSS have a much better agreement with the micro-CT image than that generated by CCSIM. Thus, it can be deduced that the CCSIM-TSS algorithm performs better than CCSIM algorithm.

3.2 Comparison and Analysis

We have compared the CCSIM-TSS and CCSIM algorithm, and in this section, we will further examine the difference of performance between the CCSIM-TSSp and CCSIM-TSSmp algorithm using the four rock samples.

The 2D images of each sample used as DIs are shown in Fig. 12. Additionally, the two-point connectivity probability function (ACF(r)) and the multiple-point connectivity probability function ($P(r)$) are calculated.

Thirty realizations are generated with CCSIM-TSSp and CCSIM-TSSmp algorithm, respectively. To compare CCSIM-TSSp with CCSIM-TSSmp quantitatively, the MDS-ANODI method are applied to the reconstructed results, see Fig. 13 and Table 5. Inspecting Fig. 13, one can see that for each sample, the CCSIM-TSSmp method has a better uncertainty space than the CCSIM-TSSp. Clearly, consistent with the plot in Fig. 13, for each sample, the space of uncertainty (between) for CCSIM-TSSp in Table 5 is smaller than CCSIM-TSSmp. At the same time, for each sample, the difference of the pattern reproduction between CCSIM-TSSmp and CCSIM-TSSp method is smaller than the difference of

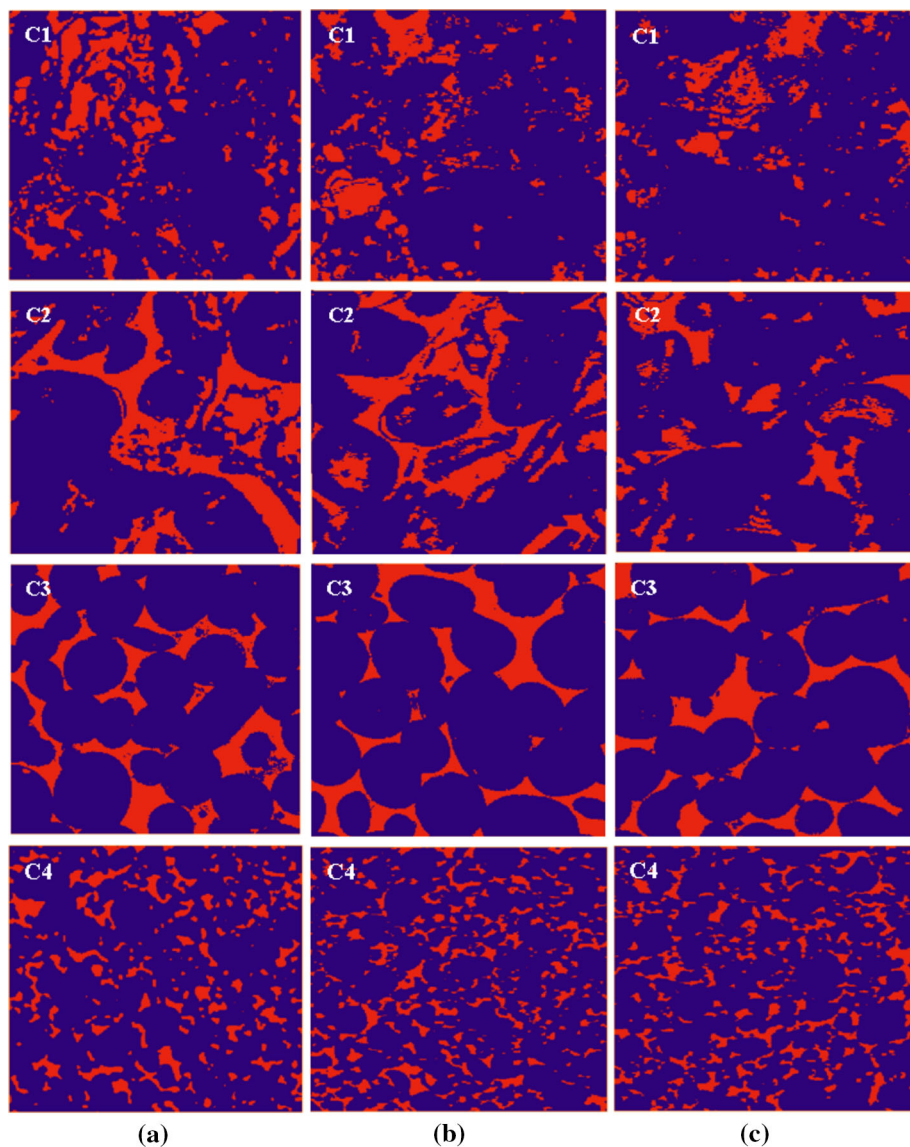


Fig. 12 The extracted 2D representative DIs in the XY (a), XZ (b) and YZ (c) plane of C1, C2, C3 and C4

space of uncertainty (Table 5). Note that an accurate method must have two features: it must produce an ensemble of realizations with significant differences between each other, while each of them is still a plausible representation of the Micro-CT image. It can be obtained from the ratio of between and within in Table 5 that the difference of the performance between CCSIM-TSStp and CCSIM-TSSmp for C3 is the biggest one in the four examples ($\gamma_{\text{CCSIM-TSSmp}}/\gamma_{\text{CCSIM-TSStp}} = 1:0.6315$), while the difference of the performance between CCSIM-TSStp and CCSIM-TSSmp for C2 is larger than that for C1. One can also notice that the performance of the two algorithms in reproducing 3D models of C4 is similar.

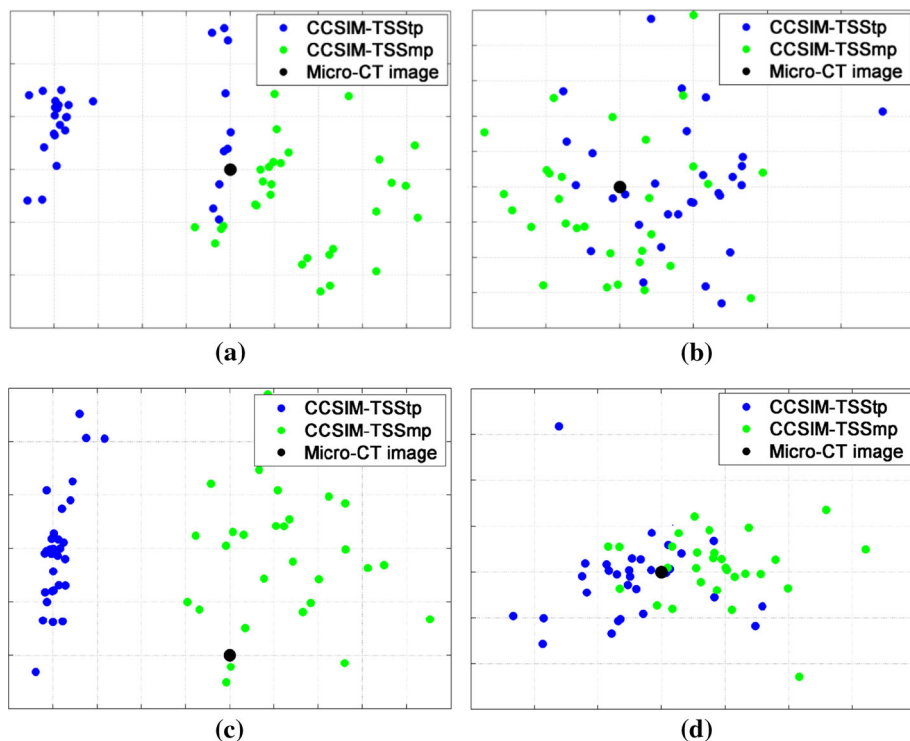


Fig. 13 The MDS-ANODI plot illustrating the spatial variability for C1 (a), C2 (b), C3 (c) and C4 (d). Realizations (shown here by blue for CCSIM-TSSmp) with better pattern reproduction are distributed around the TI (the black dot)

Table 5 The ANODI scores for the variability of within and between realizations and total ratio for the CCSIM-TSSmp and CCSIM-TSStp for C1, C2, C3 and C4

	CCSIM-TSSmp:CCSIM-TSStp			
	C1	C2	C3	C4
Space of uncertainty (between)	1:0.7606	1:0.8156	1:0.7181	1:0.9242
Pattern reproduction (within)	1:0.8175	1:1.0178	1:0.9494	1:0.9662
Ratio (between/within)	1:0.9305	1:0.8014	1:0.6315	1:0.9505

To find the trends of the difference of the performance in reproducing 3D models between CCSIM-TSStp and CCSIM-TSSmp, the ratio of $\gamma_{\text{CCSIM-TSStp}}$ and $\gamma_{\text{CCSIM-TSSmp}}$ in Table 5 are plotted versus the variance-mean ratios (signed by V) of pore-size distributions of the four rock samples, as shown in Fig. 14. Moreover, the ratio of $\gamma_{\text{CCSIM-TSStp}}$ and $\gamma_{\text{CCSIM-TSSmp}}$ is denoted as ξ ($\xi = \frac{\gamma_{\text{CCSIM-TSStp}}}{\gamma_{\text{CCSIM-TSSmp}}}$). Thus, we can obtain that the difference of the performance in reproducing 3D models between CCSIM-TSStp and CCSIM-TSSmp increases as ξ decreases. Fitting the four points (red squares), we obtain the black line in Fig. 14. The near linearity of the results confirms that the quality of the realizations generated by CCSIM-TSStp decreases rapidly as the heterogeneity of the pore space of the sample increases. This is due to the fact that, as the heterogeneity of the pore space increases, the connectivity

Fig. 14 The variance of ξ with V , ξ is the ratio of $\gamma_{\text{CCSIM-TSS}_{\text{tp}}}$ and $\gamma_{\text{CCSIM-TSS}_{\text{mp}}}$, V is the variance-mean ratios of pore-size distributions of the rock samples. The red squares are ξ of the four samples, and the black line is the fitting curves of the four red squares

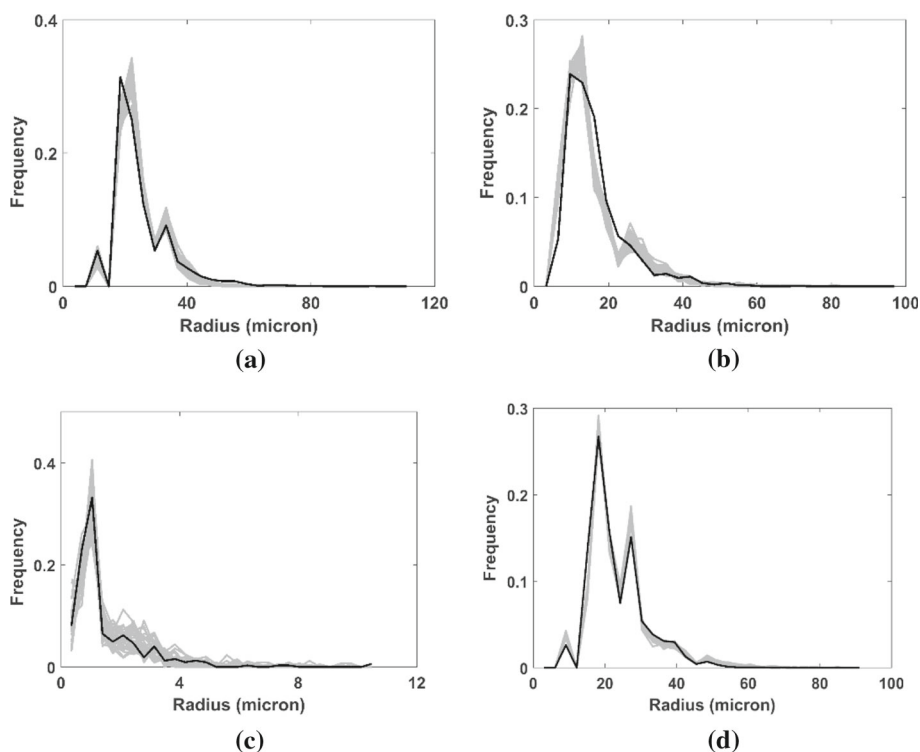
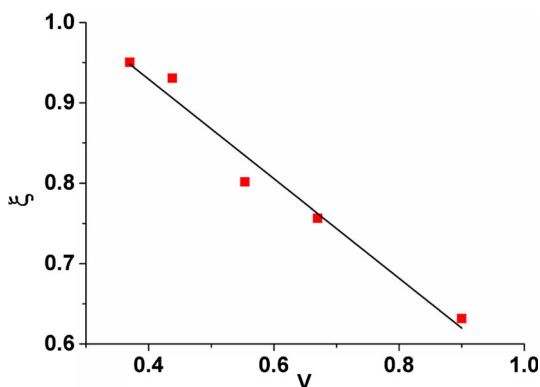


Fig. 15 The comparison of pore-size distributions of several realizations generated by CCSIM-TSSmp (gray) with those of the Micro-CT image (black) of C1 (a), C2 (b), C3 (c) and C4 (d)

becomes more complex. However, the two-point connectivity probability function is insufficient to characterize the shape and spatial continuity of complex structures. Therefore, we can obtain that the CCSIM-TSSmp algorithm performs better than CCSIM-TSS_{tp}, especially for heterogeneous porous media.

Finally, the pore-size distribution of the realizations generated by CCSIM-TSSmp are investigated. For the sake of comparison, the pore-size distributions of the realizations and the Micro-CT image of the four rock samples are plotted in Fig. 15. The results indicate a

very good agreement between the realizations and the Micro-CT image for the heterogeneous porous media.

4 Summary

In this paper, an improved method based on CCSIM and three-step sampling method-called CCSIM-TSS is proposed to reconstruct the digital core model of heterogeneous porous media. In particular, the two-point and multiple-point connectivity probability functions are used as vertical constraint conditions to preserve the long-range connectivity of the pore space. After analysis of digital rocks, some important conclusions are obtained as follows:

1. Quantitative comparison is made by computing the two-point connectivity function, absolute permeabilities and pore-size distributions for the original samples, as well as the realizations generated by CCSIM and CCSIM-TSS. The CCSIM-TSS (CCSIM-TSS_{tp} and CCSIM-TSS_{mp}) algorithm was demonstrated to be able to produce higher quality realizations than CCSIM.
2. By further comparison of the reconstructed models of CCSIM-TSS_{tp} and CCSIM-TSS_{mp}, we found that as the heterogeneity of the pore space increases, CCSIM-TSS_{mp} performs much better than CCSIM-TSS_{tp}. In other words, CCSIM-TSS_{mp} is more suitable for highly heterogeneous pore space than CCSIM-TSS_{tp}.

Acknowledgements This work is supported by the Strategic Priority Research Program of the Chinese Academy of Sciences (grant No. XDA14010304), the National Natural Science Foundation of China (Grant No. 41404114 and No. 41690132), the National Program on Key Basic Research Project (973 Program, Grant No. 2014CB239004) and the Strategic Priority Research Program of the Chinese Academy of Sciences (Grant No. XDB10020302).

Appendices

A. Two-Point Correlation Function (ACF)

The void–void (pore–pore) ACF is defined by

$$\text{ACF}(r) = \frac{E \{ [I(u) - \phi] [I(u+r) - \phi] \}}{\phi - \phi^2} \quad (\text{A-1})$$

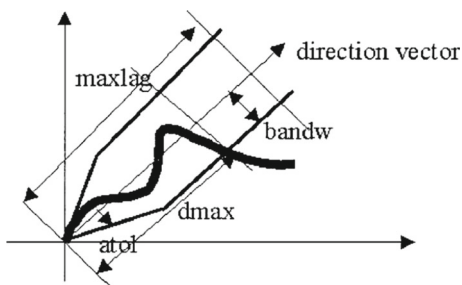
where the averaging is over all locations u within the volume, and $I(u)$ is an indicator function such that $I(u) = 1$, if u is in the pore space, and $I(u) = 0$ otherwise. The porosity is simply $\phi = E \{ I(u) \}$, $E \{ I(u) \}$ is the mean of $I(u)$ over all locations u within the volume.

B. Multiple-Point Connectivity Probability Functions

The multiple-points connectivity probability is proposed by Krishnan and Journal (2003). It is a measure of the connectivity of the system within an image. The truncated tolerance cone is defined, as shown in Fig. 16. Consider a seed location u in channel: $I(u) = 1$ (u is in the pore space). Within the defined tolerance cone, we would like to connect u through a channel path to another maximally distant location u' is in the pore space u' , that distance being measured along the axis of the cone.

More precisely, the calculation of the multiple-points connectivity probability proceeds as:

Fig. 16 The truncated tolerance cone. *bandw* is the bandwidth, controlling deviation from the central target direction at larger distances. *Maxlag* is the maximum distance



Loop through all nodes u of the study area.

- If $I(u) = 0$, set $d_{\max} = 0$ and go to next node u .
- If $I(u) = 1$, i.e., location u belongs to the pore space, call MATLAB function `bwselect` to determine within the tolerance cone with apex at u , the set (body) of all locations u' belonging to the pore space, i.e., $I(u') = 1$. Loop through all these locations u' and determine the maximum distance d_{\max} to the apex u . Increment the n proportions of continuous (and curvilinear) channel paths of length $n\bar{h} \leq d_{\max}$. \bar{h} is a unit vector in any given direction.

It should be emphasized that the tolerance angle is $\pm 22.5^\circ$, the bandwidth is 10 pixels during calculating the curvilinear directional connectivity in this paper.

References

- Biswal, B., Manwart, C., Hilfer, R., Bakke, S., Øren, P.E.: Quantitative analysis of experimental and synthetic microstructures for sedimentary rock. *Phys. A Stat. Mech. Appl.* **273**(3), 452–475 (1999)
- Biswal, B., Øren, P.E., Held, R.J., Bakke, S., Hilfer, R.: Stochastic multiscale model for carbonate rocks. *Phys. Rev. E* **75**(6), 061303 (2007)
- Bryant, S., Blunt, M.: Prediction of relative permeability in simple porous media. *Phys. Rev. A* **46**(4), 2004–2011 (1992)
- Coelho, D., Thovert, J.F., Adler, P.M.: Geometrical and transport properties of random packings of spheres and aspherical particles. *Phys. Rev. E* **55**(2), 1959–1978 (1997)
- Gao, M.L., He, X.H., Teng, Q.Z., Zuo, C., Chen, D.D.: Reconstruction of three-dimensional porous media from a single two-dimensional image using three-step sampling. *Phys. Rev. E* **91**, 013308 (2015)
- Hajizadeh, A., Farhadpour, Z.: An algorithm for 3D pore space reconstruction from a 2D image using sequential simulation and gradual deformation with the probability perturbation sampler. *Transp. Porous Med.* **94**(3), 859–881 (2012)
- Hajizadeh, A., Safekordi, A., Farhadpour, Z.: A multiple-point statistics algorithm for 3D pore space reconstruction from 2D images. *Adv. Water Resour.* **34**(10), 1256–1267 (2011)
- Hazlett, R.D.: Statistical characterization and stochastic modeling of pore networks in relation to fluid flow. *Math. Geol.* **29**(6), 801–822 (1997)
- Ioannidis, M.A., Chatzis, I., Kwiecien, M.J.: Computer enhanced core analysis for petrophysical properties. *J. Can. Pet. Technol.* **38**, 18–24 (1999)
- Krishnan, S., Journel, A.G.: Spatial connectivity: from variograms to multiple-point measures. *Math. Geol.* **5**(8), 915–925 (2003)
- Mo, X.W., Zhang, Q., Lu, J.A.: A complement optimization scheme to establish the digital core model based on the simulated annealing method. *Chin J. Geophys.* **59**(5), 1831–1838 (2016)
- Øren, P.E., Bakke, S.: Process based reconstruction of sandstones and prediction of transport properties. *Transp. Porous Med.* **46**(2–3), 311–343 (2002)
- Øren, P.E., Bakke, S.: Reconstruction of Berea sandstone and pore-scale modeling of wettability effects. *J. Pet. Sci. Eng.* **39**(2), 177–199 (2003)

- Payne, S.S., Wild, P., Lubbe, R.: An integrated solution to rock physics modeling in fractured carbonate reservoirs. In: Annual International Meeting, 80th, Society of Exploration Geophysicists. Tulsa, Okla, USA: Society of Exploration Geophysicists, vol. 1, pp. 358–362 (2010)
- Quiblier, J.A.: A new three-dimensional modeling technique for studying porous media. *J. Colloid Interface Sci.* **98**(1), 84–102 (1984)
- Strebel, S.: Conditional simulation of complex geological structures using multiple-point geostatistics. *Math. Geol.* **34**, 1–22 (2002)
- Strebel, S., Cavelius, C.: Solving speed and memory issues in multiple-point statistics simulation program SNESIM. *Math. Geol.* **46**(2), 171–186 (2014)
- Tahmasebi, P., Sahimi, M.: Enhancing multiple-point geostatistical modeling: 1. Graph theory and pattern adjustment. *Water Resour. Res.* **52**(3), 2074–2098 (2016)
- Tahmasebi, P., Hezarkhani, A., Sahimi, M.: Multiple-point geostatistical modeling based on the crosscorrelation functions. *Comput. Geosci.* **16**(3), 779–797 (2012)
- Tahmasebi, P., Javadpour, F., Sahimi, M.: Three-dimensional stochastic characterization of shale SEM images. *Transp. Porous Med.* **110**, 521–531 (2015)
- Tahmasebi, P., Javadpour, F., Sahimi, M., Piri, M.: Multiscale study for stochastic characterization of shale samples. *Adv. Water Resour.* **89**, 91–103 (2016)
- Tan, X.J., Tahmasebi, P., Caers, J.: Comparing training-image based algorithms using an analysis of distance. *Math. Geosci.* **46**, 149–169 (2014)
- Thovort, J.F., Adler, P.M.: Grain reconstruction of porous media: application to a Bentheim sandstone. *Phys. Rev. E* **83**(5), 6116–6129 (2011)
- Thovort, J.F., Yousefian, F., Spanne, P.: Grain reconstruction of porous media: application to a low-porosity Fontainebleau sandstone. *Phys. Rev. E* **63**(6), 1307–1323 (2001)
- Weger, R.J., Eberli, G.P., Baechle, G.T., Massafiero, J.L., Sun, Y.F.: Quantification of pore structure and its effect on sonic velocity and permeability in carbonates. *AAPG Bull.* **93**(10), 1297–1317 (2009)
- Yao, J., Wang, C.C., Yang, Y.F., Hu, R.R., Wang, X.: The construction of carbonate digital rock with hybrid superposition method. *J. Pet. Sci. Eng.* **110**, 263–267 (2013)
- Yi, Z.X., Lin, M., Jiang, W.B., Zhang, Z.B., Li, H.S., Gao, J.: Pore network extraction from pore space images of various porous media systems. *Water Resour. Res.* (2017). **53**(4), 3424–3445 (2017)